

Polygon construction to investigate melting in two-dimensional strongly coupled dusty plasma

W. D. Suranga Ruhunusiri,* J. Goree, Yan Feng, and Bin Liu

Department of Physics and Astronomy, The University of Iowa, Iowa City, Iowa 52242, USA

(Received 27 January 2011; revised manuscript received 15 April 2011; published 3 June 2011)

The polygon construction method of Glaser and Clark is used to characterize melting and crystallization in a two-dimensional (2D) strongly coupled dusty plasma. Using particle positions measured by video microscopy, bonds are identified by triangulation, and unusually long bonds are deleted. The resulting polygons have three or more sides. Geometrical defects, which are polygons with more than three sides, are found to proliferate during melting. Pentagons are found in liquids, where they tend to cluster with other pentagons. Quadrilaterals are a less severe defect, so that disorder can be characterized by the ratio of quadrilaterals to pentagons. This ratio is found to be less in a liquid than in a solid or a superheated solid. Another measure of disorder is the abundance of different kinds of vertices, according to the type of polygons that adjoin there. Unexpectedly, spikes are observed in the abundance of certain vertex types during rapid temperature changes. Hysteresis, revealed by a plot of a disorder parameter vs temperature, is examined to study sudden heating. The hysteresis diagram also reveals features suggesting a possibility of latent heat in the melting and rapid cooling processes.

DOI: [10.1103/PhysRevE.83.066402](https://doi.org/10.1103/PhysRevE.83.066402)

PACS number(s): 52.27.Lw, 64.60.A–, 64.60.Cn, 61.20.–p

I. INTRODUCTION

Dusty plasma consists of microparticles immersed in plasma [1–3]. In laboratory experiments the microparticles are often made of a dielectric material such as a polymer, and they can range in size from nanometers to micrometers. These microparticles collect electron and ion currents and become charged. In laboratory dusty plasma, the charge is usually negative and quite large, typically thousands of electronic charges for micrometer-size particles. Dusty plasma like this is sometimes termed complex plasma.

Due to the large charge, microparticles interacting among themselves can have potential energies larger than their kinetic energies; when this happens the microparticles comprise a strongly coupled plasma. In general, unlike more common weakly coupled plasmas, strongly coupled plasmas can exhibit the properties of liquids or solids [4] because the particles are highly collisional with their nearest neighbors. When these Coulomb interactions are so dominant that a particle is trapped by its nearest neighbors, the strongly coupled plasma acts like a solid called a Wigner crystal. The melting transition between solid-like and liquid-like phases of strongly coupled plasmas has been studied for many years. Many of the earliest melting theories and simulations were carried out assuming a $1/r$ potential, that is, the one-component plasma (OCP) model [5–10]. Experiments appeared later, when apparatus to cool and confine pure-ion plasmas was developed [11,12]. Later, simulations of melting in plasma were carried out assuming a Yukawa (Debye-Hückel) potential [13–17].

In the field of condensed matter physics, melting is often studied using model systems, which usually allow direct observation of the positions and motions of the constituent particles. A colloidal suspension is an example of a model system that allows imaging of the positions of particles, which is ideal for an experimental study of melting at an atomistic scale [18,19]. Dusty plasma can serve as another model system, and it allows imaging of particles and their motion with video

microscopy [20–22]. Dusty plasma also allows manipulation of microparticles, for example, by applying radiation pressure forces from laser beams to increase the kinetic temperature of microparticles [23,24].

One approach to study melting theoretically and experimentally is with two-dimensional (2D) systems. Melting experiments have been reported with many 2D or quasi-2D physical systems, including colloidal suspensions [25–27], electrons on liquid helium surface [28], liquid crystal films [29], vibrated granular monolayers [30], magnetic bubble arrays [31], ferrofluid spikes [32], vortex lattices in superconductors [33], and gases adsorbed on graphite surfaces [34]. Two-dimensional melting experiments have also been performed in dusty plasmas with a single layer of microparticles suspended in a glow discharge plasma [23,35–39]. Quasi-2D melting experiments have also been performed in dusty plasmas, with multiple layers [40–44].

Two-dimensional melting is often described as being mediated by defects. Defects play a central role in several theories and descriptions of 2D melting [45–51]. Identifying defects in 2D simulations, and in 2D experiments that allow direct imaging, is commonly done using Voronoi analysis [52].

Here we will use polygon construction, an alternative to Voronoi analysis developed by Glaser and Clark [49,50], to analyze melting in a 2D strongly coupled dusty plasma experiment. Beyond comparing the 2D structure in solid and liquid states, we will also explore the development of structure during rapid heating. The experiment we analyze was previously reported, along with Voronoi analysis [53]. The rapid heating that was employed in this experiment yielded a short-lived superheated solid, that is, a structure with few defects as in a solid but a temperature above the melting point. Here we will further investigate the superheated solid, exploiting the sensitivity of polygon construction.

We provide our source code for polygon construction in the supplementary material [54]. Our intention is to encourage readers to use it for other experiments or simulations. We have validated this code by testing it using a simulation with the same WCA potential as in [50] to verify

*suranga-ruhunusiri@uiowa.edu

that we obtain the same results (within statistical uncertainty) for the abundance of various polygons. We carried out these tests using the same temperature and density parameters as in [50].

In Sec. II we review the motivation and method for polygon construction, and compare it to Voronoi analysis. The experiment and data analysis procedure are summarized in Sec. III. In Sec. IV we present and interpret our results.

II. DEFECT IDENTIFICATION

A common way of identifying defects in 2D systems is an analysis of coordination number, that is, the number of nearest neighbors. This starts with measurement of positions of individual particles [Fig. 1(a)]. Next, a map of bonds between particles [Fig. 1(b)] is calculated by a Delaunay triangulation. This map consists of triangles that fill the plane with a vertex located at the position of each particle. The number of bonds at a vertex is the coordination number. One can, as an additional step, draw perpendicular bisectors of the bonds, yielding a polygon map called a Voronoi diagram [Fig. 1(c)]. A perfect 2D lattice consists of triangles with hexagonal symmetry, and in such a perfect lattice, the Voronoi polygons are all six sided. Defects are identified as non-six-sided polygons, with five- or seven-sided polygons being the most common. Two common defect types are the disclination (which is identified by a single non-sixfold polygon) and a dislocation (which is identified by a pair of disclinations, one with five sides and the other with seven), as seen in Fig. 1(c). The number of sides in a Voronoi polygon corresponds to the number of nearest neighbors, that is, coordination number. In this paper we will use the term Voronoi analysis in a general sense to include methods of analyzing coordination number with or without drawing Voronoi polygons. Voronoi analysis has been used in 2D colloid experiments [25–27,55,56] and in many dusty plasma experiments, not only for planar 2D suspensions [38–43,57,58] but also for surfaces in 3D suspensions [59].

Polygon construction [49,50] is a different way of characterizing defects in a 2D structure with polygons. Like Voronoi polygons, these polygons form a network that covers the entire plane [Fig. 1(d)]. Unlike Voronoi polygons, however, the sides of these polygons coincide with bonds identified by triangulation, and there are usually fewer sides in the polygon. While defects play a central role in both polygon construction and Voronoi analysis, there are differences in the type of defects that are identified and their significance. Geometrical defects are identified in polygon construction, whereas topological defects are identified by Voronoi analysis. In the polygon construction method, polygons with four or more sides are the geometrical defects. In Voronoi analysis, non-six-sided Voronoi polygons are the topological defects. These two types of defects do not have a one-to-one correspondence, as we discuss below.

Glaser and Clark took the approach that an understanding of melting requires an understanding of liquid structure. They were motivated by Bernal [60,61] who compared solid and liquid structure by identifying excess volumes in the packing of hard spheres. These excess volumes, which correspond to a local nontriangular packing, are especially common in 2D liquids. For example, if four nearby particles are arranged so

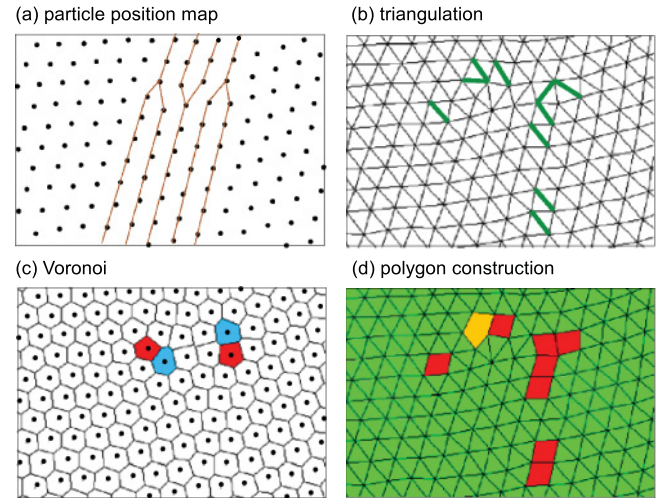


FIG. 1. (Color online) A particle position map (a) produced by analyzing an experimental image. This is used to construct a triangulation map (b), which indicates bonds. The triangulation map can be used to compute a Voronoi diagram (c), which depicts topological defects, which are non-six-sided cells shown shaded. By removing bonds that are opposite large angles from the triangulation map, marked by bold lines in (b), we obtain the polygon construction (d). Non-three-sided polygons in (d) indicate geometrical defects, which do not have a one-to-one correspondence with the topological defects in (c).

that their bonds are 90° , there will be a larger empty volume between them than if they were 60° . Larger empty volumes like these appear often in the 2D-liquid structure. Glaser and Clark’s polygon construction identifies these excess volumes and categorizes them according to the number of particles that surround them.

Polygon construction starts with the same inputs as Voronoi analysis: measurements of positions of individual particles and a map of bonds. To identify excluded volumes using this triangulation map, certain bonds are removed so that for example two adjoining triangles are redrawn as a quadrilateral. There are two practical approaches for this identification: either remove an unusually long bond (which corresponds for example to the diagonal of a quadrilateral) or identify a bond that is opposite an unusually large angle between two of the adjoining bonds. To illustrate this we have marked the bonds selected by the latter approach in Fig. 1(b). Removing these bonds yields the desired polygons, which can have four or more sides [Fig. 1(d)]. This construction resembles a tiling, except that the tiles are not exactly the same; they are individually deformed so that their vertices coincide with particle locations. We also note that this construction eliminates an ambiguity that could occur in Delaunay triangulation, as we explain in the Appendix.

The two types of defects measured by Voronoi analysis and polygon construction are different. In Fig. 1 we see that the geometrical defects identified by polygon construction do not necessarily coincide with the positions of geometrical defects identified by Voronoi analysis. For example, five to seven disclination pairs in the Voronoi analysis [Fig. 1(c)] are dislocations, that is, topological defects where rows of particles terminate. Dislocations in a Voronoi diagram often

appear near clusters of quadrilaterals or pentagons in a polygon construction, but there is no unique one-to-one relationship between the topological and geometrical defects. Moreover, in polygon construction, quadrilaterals can appear where there is some small distortion of the lattice far away from any topological defects, as seen at the bottom of Fig. 1(d), and the abundance of these quadrilaterals depends on the thresholds chosen for removing bonds.

The polygon construction method has the advantage of providing a gradation in the severity of geometrical defects. Quadrilaterals are the least severe, while pentagons, hexagons, etc. are progressively more severe. In contrast, defect identification using Voronoi analysis is usually a binary measure when used in dusty plasma experiments, that is, at the location of a particle, there is either a topological defect, or there is not [42,53]. The gradation of defects in polygon construction allows a greater sensitivity in identifying and classifying disorder.

Although the polygon construction method has some advantages when compared to Voronoi analysis, its use has not yet become common. We find only two previous reports of its use in the literature. It was introduced with 2D simulations [49,50], and it was later used in an experiment with Cs atoms, which were adsorbed on a Si-Ag surface, and imaged by scanning tunneling microscopy [62].

III. EXPERIMENT AND ANALYSIS

The dusty plasma experiment that we analyze was first reported in [53], where it was analyzed by the Voronoi method. We briefly summarize the experimental conditions and procedures here; further details are provided in [53], and the apparatus is described in [24]. The dusty plasma is a four-component mixture of neutral gas, positive argon ions, electrons, and electrically charged microparticles. Argon gas at 7 mTorr was partially ionized by applying a low power rf voltage at 13.56 MHz with a 97 V peak-to-peak amplitude. Monodisperse melamine formaldehyde microparticles of diameter $4.83 \mu\text{m}$ were introduced into the plasma. The mutual repulsion of these microparticles in the experiment can be modeled by a Yukawa potential [63], with $-4360e$ for the electrical charge and 0.65 mm for the screening length. The microparticles were levitated in an electric sheath above the lower electrode. By limiting the number of microparticles inserted into the plasma, a suspension was prepared with only a single layer and a lattice constant $b = 0.86 \text{ mm}$. In the absence of manipulation, the microparticles self-organized in a solid triangular lattice with sixfold symmetry.

Particle motion was tracked using video microscopy. A digital camera operated at 55 frames/s imaged a $34.2 \times 25.6 \text{ mm}^2$ region that contained about 1000 microparticles. The particle positions, which are the starting point for our polygon construction, were measured using an image analysis procedure [64] for each particle in each video frame.

The experimenters controlled the kinetic temperature, which describes the kinetic energy of random motion of the microparticles. This kinetic temperature is not a thermodynamic temperature because the surrounding gas and plasma had different temperatures. The polymer material inside the microparticles probably had yet another temperature that was

never hot enough to melt them. The melting that we study in this paper is not for the polymer material itself, but rather for the spatial configuration of microparticles that are suspended in space.

The kinetic temperature was increased suddenly to cause melting by abruptly applying laser manipulation. This laser manipulation, which applied nearly random kicks to microparticles [24], was sustained for 55 s. Afterwards, laser heating was abruptly turned off to allow a cooling due to gas friction. The resulting time series for kinetic temperature is shown in Fig. 2(a). In general, a melting point could be identified several ways. We choose to use the phase diagram of Hartmann *et al.* [17]. They identified the melting point by noting a sharp decay of the bond-angular order parameter as temperature was varied slowly in their 2D Yukawa simulation.

In polygon construction it is necessary to define a somewhat arbitrary threshold when identifying unusually long bonds or unusually large angles for bond removal. For bond length, the threshold should be between b and $\sqrt{2}b$ (where b is the lattice constant for a perfect triangular lattice) in order to identify quadrilateral arrangements. For bond angles, the threshold should be between 60° and 90° , again to allow identifying quadrilateral arrangements. Here we use the bond-angle approach, with the same 75° threshold as in [49,50].

We use this polygon construction three ways. First, to determine how defects proliferate and cluster as melting progresses, we inspect maps visually. Second, to characterize disorder during the formation of a superheated solid and subsequent melting, we count types of polygons, for example, triangles and quadrilaterals. Third, to quantify our observations of how defects tend to cluster, we will classify each vertex according to the sequence of polygons around the vertex.

IV. RESULTS AND CONCLUSIONS

A. Comparing the structures of liquid and solid

Geometrical defects proliferate when sudden laser heating is applied, and then diminish after laser heating is stopped, as seen in Figs. 2(b)–2(g). Initially, before applying laser heating, the collection of particles in the suspension had the structure of a solid. The polygon construction for this solid consists mainly of triangles [Fig. 2(b)]. Next, during the application of laser heating, particles move and nontriangular polygons proliferate in Figs. 2(c) and 2(d). During the cooling immediately after the laser heating stopped, nontriangular polygons diminish in Figs. 2(e) and 2(f). Finally, after the kinetic temperature drops to its original value, we find that the geometrical defects in the structure slowly become less numerous [Fig. 2(g)].

To identify which polygon types proliferate the most during heating, we quantify them with order parameters P_3 , P_4 , P_5 , and P_6 . These order parameters, defined by Glaser and Clark [50], are a measure of the abundance of a particular polygon type. For example, P_3 and P_4 are the respective number of triangles and quadrilaterals, normalized by $2N$, where N is the number of analyzed particles. Time series results for these order parameters are presented in Fig. 3.

These time series reveal that when comparing a liquid to a solid, quadrilaterals are the most abundant geometrical defect, followed by pentagons and hexagons. This ordering

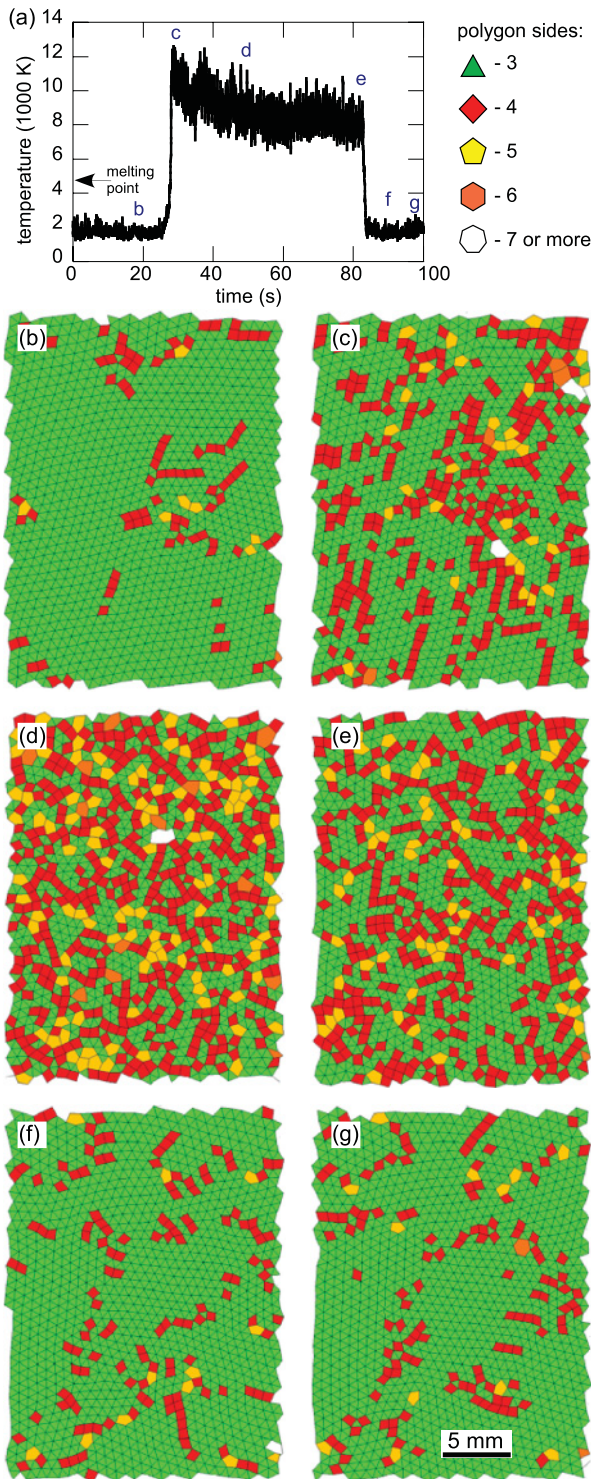


FIG. 2. (Color online) Results from an analysis of the sudden-heating experiment of [53]. Starting with a low-temperature solid structure, laser heating was suddenly applied and then later turned off. (a) Time series of microparticle kinetic temperature reported in [53]. Times marked b–g correspond to the panels below. (b)–(g) Polygon construction: triangles are non-defects, while quadrilaterals, pentagons, hexagons, etc. are geometrical defects. Starting with a solid (b), after laser heating was turned on a proliferation of geometrical defects is seen during melting, (c) and (d). Diminishment of geometrical defects is seen during cooling, (e)–(g), as crystallization gradually progresses.

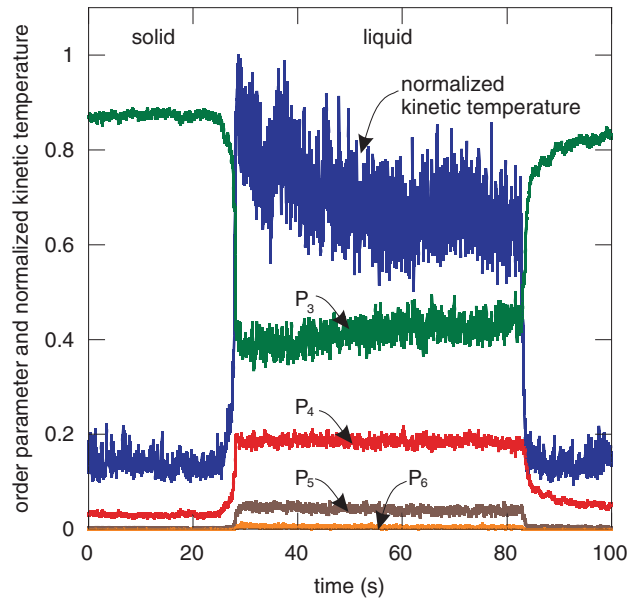


FIG. 3. (Color online) Time series for order parameters P_3 to P_6 and the kinetic temperature (normalized by its maximum). The abundance of geometrical defects, as indicated by P_4 to P_6 , is greater in a liquid than in the initial solid. Quadrilaterals, indicated by P_4 , are the most frequent geometrical defect (in both a liquid and a solid), while pentagons and hexagons are the next most frequent.

is as expected, since quadrilaterals are the least severe type of geometrical defect. A similar ordering was observed in WCA simulations [49,50]. Later, we will characterize the ratio P_4/P_5 , which reveals the relative abundance of these two kinds of geometrical defects.

We find that geometrical defects in strongly coupled dusty plasma tend to cluster, so that a polygon tends to be adjacent to another polygon of the same type. For example, quadrilaterals tend to adjoin other quadrilaterals, as was noticed previously by Glaser and Clark in their WCA simulations [49–51]. This tendency of quadrilaterals to cluster is noticeable in both our solid [Fig. 4(a)] and our liquid [Fig. 4(b)]. Additionally, in the liquid we observe that pentagons tends to cluster with other pentagons, as can be seen in Fig. 4(b).

When quadrilaterals cluster with one another, the result is often a ladder-like structure. Examples for our experiment are

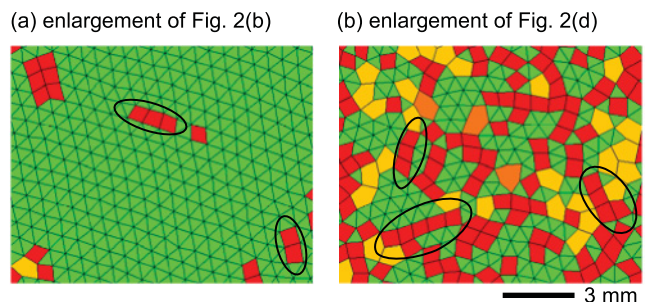


FIG. 4. (Color online) Enlargements (a) of Fig. 2(b) for the initial solid and (b) Fig. 2(d) for a liquid. Quadrilaterals tend to cluster with other quadrilaterals, often forming ladder-like structures like the examples encircled here. Likewise, pentagons tend to cluster with other pentagons, as seen in (b).

Vertex type	Diagram	Vertex type	Diagram	Vertex type	Diagram	Vertex type	Diagram
A		D		G		J	
B		E		H		K	
C		F		I		L	

FIG. 5. (Color online) The first 12 vertex types, among the 25 classified in [50]. Vertices are at the locations of particles. In a perfect 2D crystal, only type *A* would be found.

circled in Fig. 4(a) for a solid and Fig. 4(b) in a liquid. These ladder-like structures are often linear, but sometimes they bend or branch. Similar structures were observed in a WCA liquid simulation [49–51].

To classify how polygons adjoin, we use the vertex classification scheme of Glaser and Clark [50]. They identified 25 common configurations of polygons arranged around a vertex, and labeled them with the letters *A–Y*. Some of the vertex types that occur most frequently are sketched in Fig. 5. In a perfect crystal, one would observe only vertex type *A*, where six triangles join.

To quantify the abundance of vertex types, we calculate the vertex fraction [50], which is the ratio of vertices of a certain type to the total number of vertices in the polygon construction. For example, in Fig. 2(b) we count 62 occurrences of vertex type *B*, and 1066 total vertices, so that we calculate the vertex fraction for type *B* as $62/1066 = 0.058$.

Under steady conditions, we find that in the dusty plasma, the vertex fractions are quite different in the solid and the liquid [Fig. 6(a)]. Vertex type *A* is the most common in our solid, but not in our liquid. The most common vertices in our liquid are *B*, *C*, *E*, *F*, and *G*, in that order. All those vertex types include a geometrical defect, and they are all more common than *A* in our liquid. It is interesting also to compare our vertex fractions to those of the WCA potential, because the interparticle potentials are different. Using the WCA simulation data from [50], we prepared Fig. 6(b). We find that in a liquid the vertex fraction for type *A* is much smaller in our dusty plasma experiment than in the WCA liquid. The other vertex fractions are generally more abundant in our liquid, especially *D*, *G*, *H*, *P*, *S*, and *W*, which have a vertex fraction in our experiment that is at least double that of the WCA liquid.

When heating was abruptly turned on and off in the experiment, we observe some unexpected transients in the vertex fractions. The time series for vertex fractions (Fig. 7) reveal that while some of the non-*A* vertex types become gradually more abundant as the temperature is increased, others do not. Vertex fractions for types such as *C* and *D* increase monotonically with temperature, but those for *E* and *F* (and to a lesser extent *B*) have prominent spikes near the times that heating was turned on and off.

We can suggest two possible explanations for these transient spikes. Perhaps vertex types *E* and *F* are metastable states, with an intrinsic time dependence during both melting and

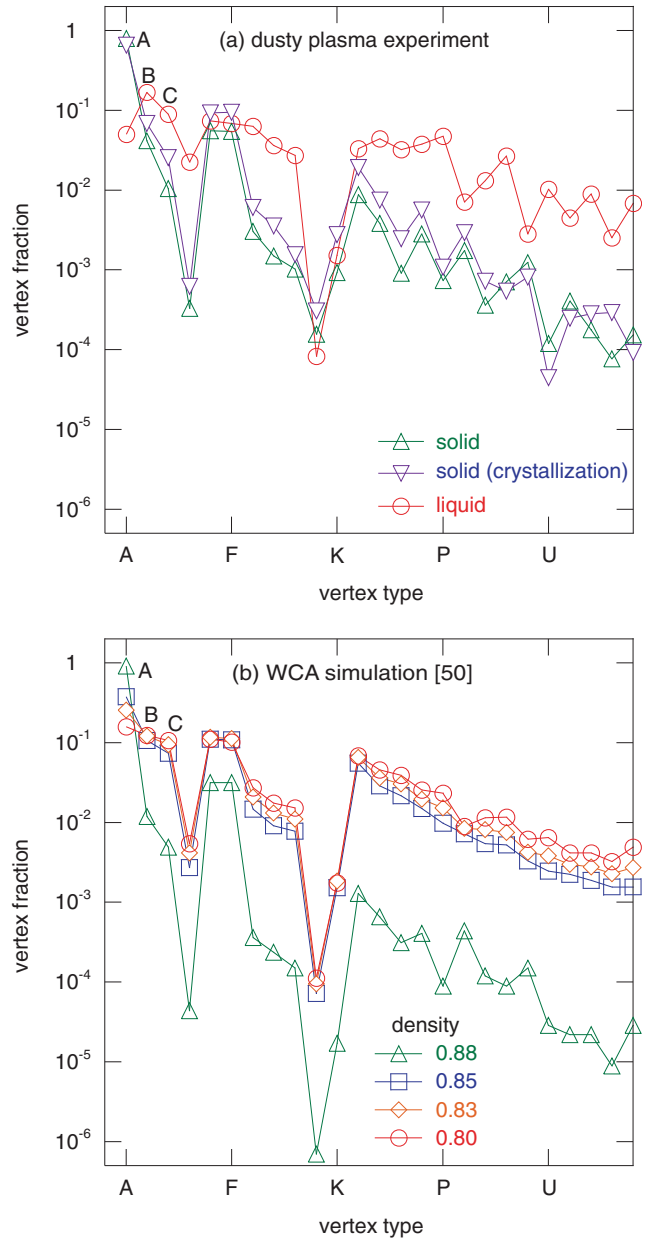


FIG. 6. (Color online) Vertex fraction, calculated as the number of observations of a particular vertex type such as *A* or *B*, divided by the total number of vertices observed. (a) Dusty plasma experimental data. Error bars based on counting statistics are too small to plot. Many video frames were used in the calculation: 1000 frames for the solid, 2000 for the liquid, and 500 for the solid undergoing crystallization. The latter is for the time interval 92.2–100 s. (b) Data from Table I of Glaser and Clark’s simulation of a 2D WCA system [50], where density was varied instead of temperature. Densities of 0.88 and 0.80 correspond to a solid near melting and a liquid near freezing, respectively. Lower densities of 0.85 and 0.83 correspond to dense liquids.

solidification. Alternatively, *E* and *F* might have no particular time dependence and they might occur only in a narrow range of temperature. Further studies, comparing results with both slowly and rapidly varying temperature, would be helpful in determining the special nature of vertex types *E* and *F*.

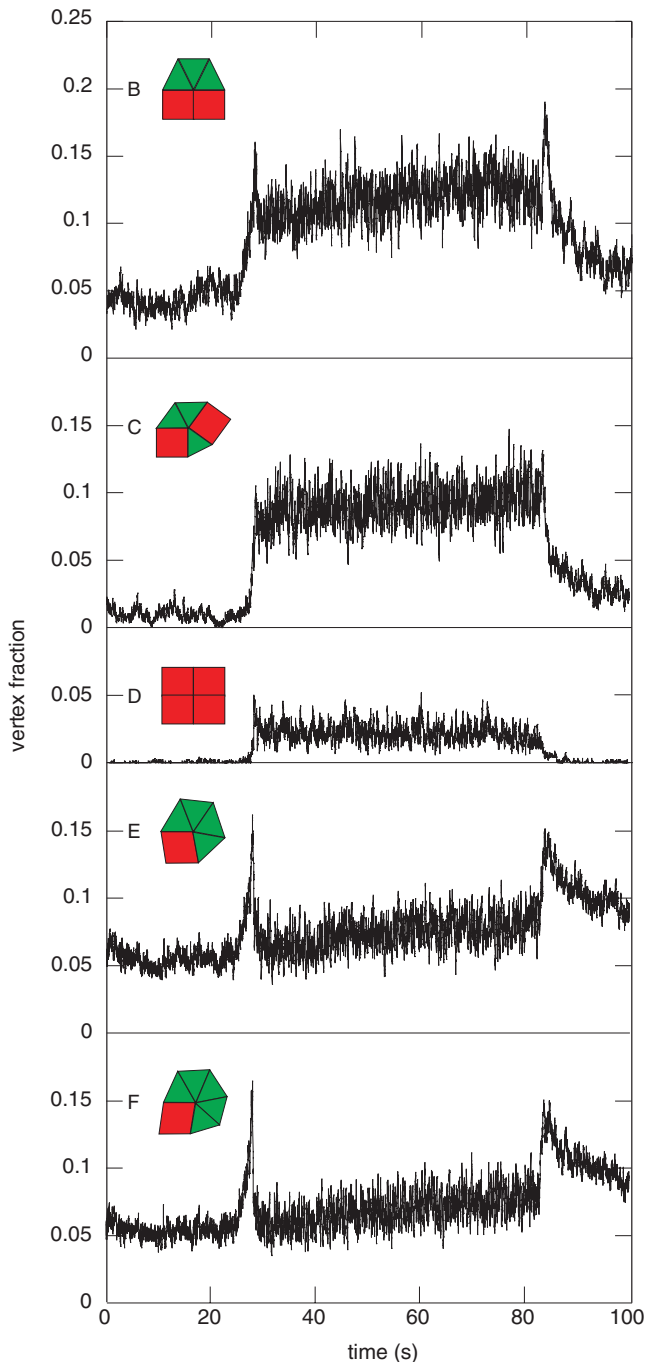


FIG. 7. (Color online) Time series of vertex fractions for the experiment. The vertex types shown contain at least one geometrical defect. Some but not all of these vertex types are more common in a liquid than a solid. Unexpectedly, for vertex type *B*, spikes appear during sudden heating and again when laser heating is turned off. More prominent spikes appear for vertex types *E* and *F* during sudden heating, and again when laser heating is turned off, but during steady conditions these vertex fractions are nearly the same in our initial solid and the liquid.

B. Hysteresis diagrams

One can combine two time series, the kinetic temperature and a measure of disorder, to prepare a hysteresis diagram. In [53] this was done using, as the measure of disorder, the

defect fraction computed by counting defects in a Voronoi diagram. Here we do the same, but with a different measure of disorder based on polygon construction. We calculate this disorder parameter as $P_4 + P_5 + P_6$. Results for the hysteresis diagrams are shown in Fig. 8(a) for the defect fraction based on Voronoi analysis, and in Fig. 8(b) for $P_4 + P_5 + P_6$ based on polygon construction. In both kinds of hysteresis diagrams features are visible that indicate solid superheating and the development of crystallization. Additionally, the hysteresis diagram in Fig. 8(b) also reveals a pair of previously unremarked features: one marked \mathbb{H} that occurs during sudden heating and one marked \mathbb{C} that is seen during the early stages of cooling after the heating is turned off. We discuss these results in detail.

C. Solid superheating

A superheated solid has the structure of a solid at a temperature above the melting point. Superheating can be achieved by two methods: suppressing surface melting or transferring a large amount of energy to a bulk solid in a brief time. The latter method was used in the experiment analyzed here [53].

At the start of the experiment, the structure is solid, in the lower left corner of the hysteresis diagram (Fig. 8). When laser heating was applied, the kinetic temperature increases, ultimately leading to a liquid in the upper right corner. Later, during cooling, the temperature diminishes and the structure gradually crystallizes, eventually returning to the solid condition in the lower left corner. The signature of a superheated solid is a horizontal row of data points after the temperature exceeds the melting point, and this is identifiable in both hysteresis diagrams, as indicated by the broken lines in Figs. 8(a) and 8(b). After the brief lifetime of the superheated solid, melting is completed with a rapid increase in disorder but little further increase in temperature.

Polygon construction allows us to expand what was known about the structure of a superheated solid. From our experiments, we find that despite having more defects than a solid, a superheated solid has quadrilateral and pentagon defects with proportions that are like those for a solid, not a liquid. This is shown in the time series of the quadrilateral to pentagon ratio (Fig. 9). We expect this ratio to have a smaller value as disorder increases, due to an increased proportion of pentagons as compared to the less severe quadrilaterals. In Fig. 9 this ratio is indeed much smaller for a liquid than for a solid. What is interesting is that during the time interval of a superheated solid, this ratio is almost the same as for a solid, not a liquid. Thus, we conclude that the defect structure of a superheated solid more closely resembles that of a solid than a liquid.

D. Crystallization

We can study crystallization by examining the development after turning off laser heating. First there was a period of rapid cooling, then crystallization. During crystallization, the random kinetic energy remains nearly constant at a level, below the melting point, and defects gradually diminish. Here we report the results for vertex fractions during crystallization in comparison to steady states, solid and liquid.

Comparing the vertex fractions during crystallization vs the original solid [Fig. 6(a)] reveals that the fractions for vertex

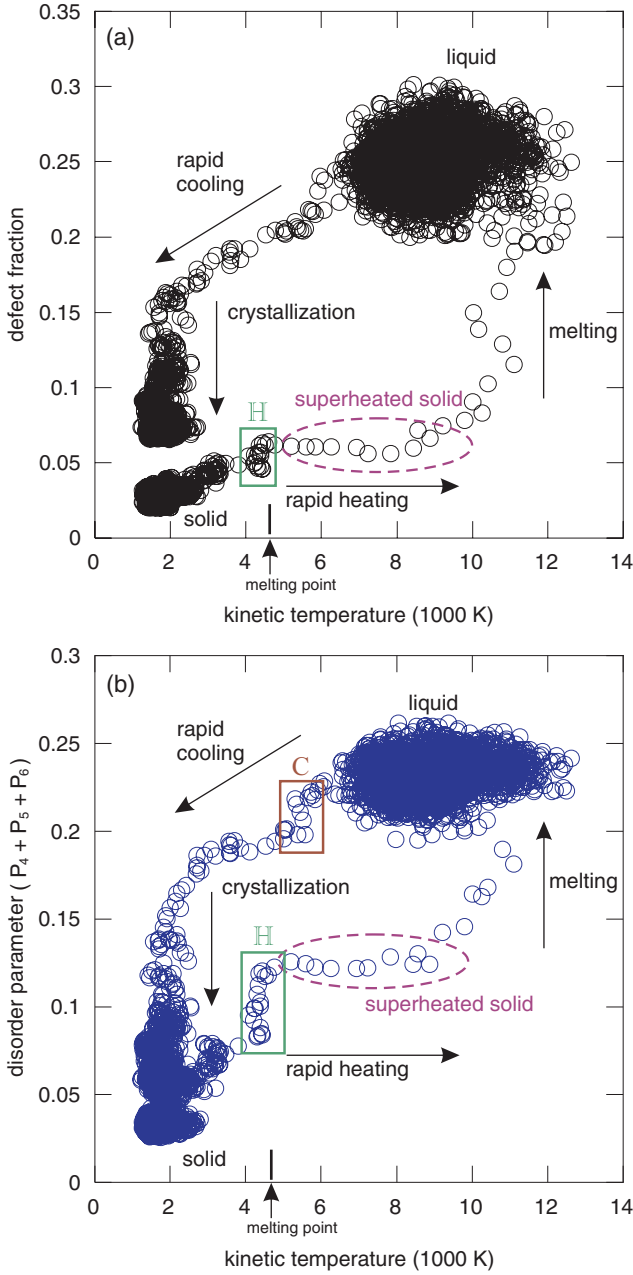


FIG. 8. (Color online) Hysteresis diagrams from combining a time series for kinetic temperature and a time series of a measure of disorder. Each data point corresponds to one video frame. (a) Hysteresis, as it was computed from Voronoi diagrams in [53], reveals a superheated solid when rapid heating commences, as indicated by the broken circle. (The defect fraction was calculated as the ratio of the area filled by five- and seven-sided Voronoi polygons to the total area.) (b) Hysteresis, as computed from polygon construction diagrams, reveals additional features. Here, the time series for the disorder parameter $P_4 + P_5 + P_6$ was combined with the time series for kinetic temperature. We note two previously unremarked features marked \mathbb{H} and \mathbb{C} . Observing these unremarked features, which are less prominent in (a), was made possible by the greater sensitivity of the polygon construction method.

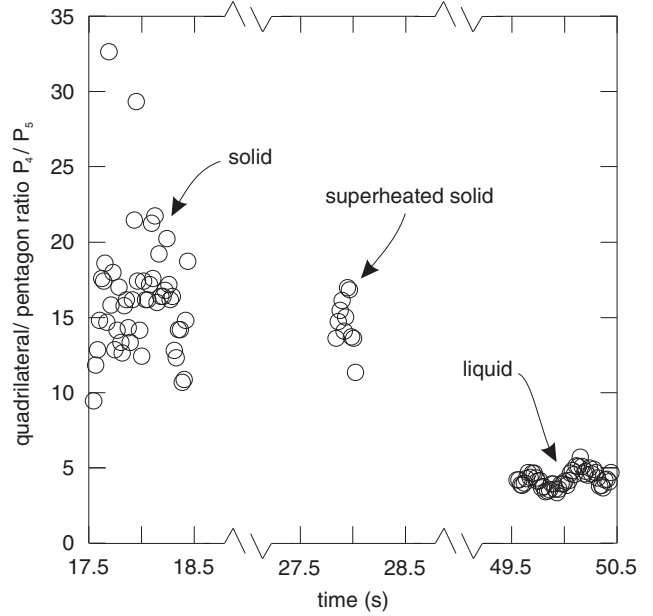


FIG. 9. Samples of the time series for P_4/P_5 . This ratio diminishes as pentagons (which are a more severe geometrical defect) become more abundant as compared to quadrilaterals. Each data point here corresponds to one video frame. As judged by this measure of defect severity, a superheated solid more closely resembles a solid than a liquid.

types $B-R$ are higher during crystallization than in the steady-state solid. Only a few vertex types that contain pentagons ($S, T, U, V,$ and Y) are more abundant during crystallization than in a solid. Vertex type A , of course, is the most common in a solid, and we have verified that its vertex fraction increases with time during crystallization.

Hartmann *et al.* [65] performed an experiment with a similar 2D dusty plasma and found that crystallization occurred with two time scales: a short one dominated by individual particle motion and a longer one where crystallites undergo collective rearrangement. Our data for crystallization in Fig. 6(a) correspond to the longer of the two time scales.

E. Hysteresis features for sudden temperature changes

Two previously unremarked features can be observed in the polygon-construction hysteresis diagram [Fig. 8(b)]. The first feature is an upward row of data points marked \mathbb{H} that is observed in the sudden heating process. The second feature is a downward row of data points marked \mathbb{C} that is observed during the cooling process. Both of these features appear near the melting point, where there is a significant change of disorder parameter without much change in kinetic temperature. First we will comment upon the reasons why these two features have a profound signature in the polygon-construction hysteresis diagram [Fig. 8(b)] compared to the Voronoi hysteresis diagram [Fig. 8(a)]. Then we discuss the physical significance of these features.

The previously unremarked features \mathbb{H} and \mathbb{C} are visible with a more profound signature when the hysteresis diagram is prepared using a measure of disorder on polygon construction [Fig. 8(b)]. We attribute the clarity in detecting these features

to the sensitivity of the polygon construction method due to the gradations of geometrical defects as compared to the more binary measure of the presence of topological defect.

Feature \mathbb{H} in the sudden heating process suggests that (at least in this experiment) sudden melting is a three-step process. First, when the temperature has reached the melting point in the experiment, there is a marked increase in disorder without any temperature increase, as indicated by the vertical row of data points enclosed by a box. Second, there is a superheated solid, revealed by a horizontal row of data points. Third, the superheated solid melts with little further increase in temperature, and this appears as another vertical row of data points.

Both features \mathbb{H} and \mathbb{C} appear as vertical rows of data points in Fig. 8(b), suggesting that the underlying physical process may involve a latent heat, which would be an indication of a first-order melting transition. In general, the latent heat in a first-order transition corresponds to a change in internal potential energy, that is, the potential energy for interparticle interactions, without a change in temperature. Our disorder parameter serves as an indirect indication of a change in the potential energy landscape. To make a definitive conclusion of whether these features indicate a first-order transition would require measurements of other thermodynamic quantities such as the internal potential energy of the system.

Perhaps one reason that feature \mathbb{H} has not been previously remarked upon is that earlier solid-superheating experiments did not allow the preparation of a hysteresis diagram like Fig. 8(b). This diagram requires data for both structure and kinetic temperature. Previous solid-superheating experiments relied on diagnostics, for example electron diffraction, that indicate structure but provide no time-resolved data for kinetic temperature. Thus, at present it is not known whether feature \mathbb{H} is common to physical systems other than dusty plasmas.

One might ask whether feature \mathbb{H} in the sudden heating process is related to the formation of the metastable states, vertex types E and F that we detected in the time series for vertex fractions (Fig. 7). Feature \mathbb{H} occurs from 27.5 to 27.8 s, whereas the spikes for vertex types E and F in Fig. 7 are observed later during sudden heating at 27.95 and 28.04 s, respectively. This suggests that feature \mathbb{H} is not related to the formation of metastable states.

We have not yet identified any special features in the structure while feature \mathbb{C} occurs, during cooling. Certainly the abundances of the different polygons changes during feature \mathbb{C} , as indicated by the value of $P_4 + P_5 + P_6$ in Fig. 8(b). However, we determine by a qualitative inspection of polygon constructions, during the time interval corresponding to feature \mathbb{C} , that there were not any other developments, such as the formation of crystallites.

V. SUMMARY

The polygon construction method of identifying geometrical defects in 2D structures is used to analyze data from a strongly coupled dusty plasma experiment in several conditions: a solid, a superheated solid during rapid heating, a liquid, and a solid undergoing crystallization. We exploit the advantage of polygon construction that it distinguishes defects according to severity.

Comparing solids and liquids under steady conditions, we find that while both quadrilaterals and pentagons become more numerous in a liquid, their ratio does not remain constant. We find that the quadrilaterals tend to cluster with other quadrilaterals in ladder-like structures in both our solid and liquid. We also find that the pentagons tend to cluster with other pentagons in our liquid. In order to classify the arrangement of polygons, we measure the vertex fractions. We find that almost all vertex types, except for type A which is typical for a hexagonal crystal, become more numerous in a liquid as compared to a solid.

The hysteresis diagram we prepared from the polygon construction suggests that sudden heating has three steps. First, at a temperature near the melting point, there is an increase in disorder without much change in temperature. Second, a superheated solid appears at temperatures above the melting point. Third, the superheated solid melts, yielding a liquid. The first of these three steps was not remarked upon previously, when a hysteresis diagram was prepared using Voronoi analysis. Further experiments or simulations are needed to determine whether this step commonly occurs during sudden heating.

Finally, polygon construction is used to characterize the nature of geometrical defects present during the transient conditions of solid superheating and crystallization. Geometrical defects in a superheated solid are more numerous than in a solid, and less numerous than in a liquid. We find that the nature of the geometrical defects in the superheated solid more closely resembles that of a solid than a liquid. This conclusion was made possible by polygon construction, which allows a calculation of the ratio of quadrilaterals (which are less severe geometrical defects) to pentagons (which are more severe).

Additionally, we also observe a transient burst in the abundance of certain vertex types during rapid changes of temperature, for both heating and cooling. The vertex types that exhibit the most profound bursts are E and F , which each contain a single quadrilateral. Further studies are needed to determine whether these vertex types are abundant only in a narrow temperature range, or whether they are a metastable configuration with a short lifetime.

ACKNOWLEDGMENTS

We thank N. A. Clark for suggesting the use of polygon construction with dusty plasma experiments and we thank M. A. Glaser for helpful discussions. This work was supported by NSF and NASA.

APPENDIX: TRIANGULATION

Polygon construction starts with measurements of individual particle positions and map of bonds calculated by Delaunay triangulation. Particle positions correspond to vertices in the triangulation and bonds correspond to the lines drawn between these vertices. Delaunay triangulation usually identifies bonds uniquely for a given configuration of particle positions. But under extremely rare circumstances it is possible for this bond calculation to be ambiguous. Here we discuss this ambiguity in Delaunay triangulation and discuss how it does not affect polygon construction.

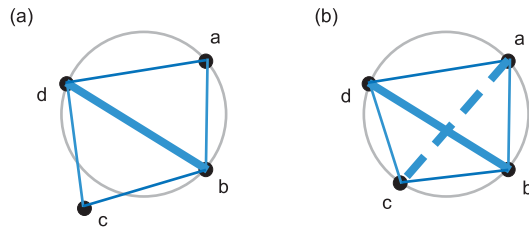


FIG. 10. (Color online) Sketch of four vertices arranged nearly in a square. (a) Usually a small circle (circumcircle) can be drawn so that it passes through only three vertices. (b) Uncommonly, the circumcircle passes exactly through four vertices, so that Delaunay triangulation has two possible outcomes, one with bond ac and the other with bd .

Bonds are calculated by Delaunay triangulation which includes a criterion that no vertex should lie inside a circle that passes through any other three vertices. A circle passing through each of the three vertices of a triangle is a circumcircle of that triangle. For example, consider the arrangement of

four particles in Fig. 10(a). The circle is the circumcircle of triangle abd and vertex c lies outside. In this case, Delaunay triangulation has a unique solution.

Ambiguity of bonds calculated from Delaunay triangulation arises when a fourth vertex lies exactly on the circumcircle of a triangle. For example, consider the vertex arrangement in Fig. 10(b), where vertex c lies on the circumcircle of triangle abd . In this instance, Delaunay triangulation may yield two different diagrams, one with bond bd shown with a solid line, and the other with a bond ac shown with a dashed line.

Polygon construction is not sensitive to this ambiguity because ambiguous bonds in Delaunay triangulation are generally long, and long bonds are removed in polygon construction. In Fig. 10(b) both of the ambiguous bonds and bd are longer than the other bonds, and they are opposite angles that are larger than our threshold angle. Thus, both ac and bd would be removed in the polygon construction. This illustrates an advantage of polygon construction: its outcome is unambiguous, even when Delaunay triangulation is ambiguous.

-
- [1] P. K. Shukla and A. A. Mamun, *Introduction to Dusty Plasma Physics* (Institute of Physics, Bristol, 2002).
- [2] G. E. Morfill and A. V. Ivlev, *Rev. Mod. Phys.* **81**, 1353 (2009).
- [3] A. Piel, *Plasma Physics: An Introduction to Laboratory, Space, and Fusion Plasmas* (Springer, New York, 2010).
- [4] S. Ichimaru, *Rev. Mod. Phys.* **54**, 1017 (1982).
- [5] J. P. Hansen, *Phys. Lett. A* **41**, 213 (1972).
- [6] E. L. Pollock and J. P. Hansen, *Phys. Rev. A* **8**, 3110 (1973).
- [7] R. C. Gann, S. Chakravarty, and G. V. Chester, *Phys. Rev. B* **20**, 326 (1979).
- [8] W. L. Slattery, G. D. Doolen, and H. E. DeWitt, *Phys. Rev. A* **21**, 2087 (1980).
- [9] Ph. Choquard and J. Clerouin, *Phys. Rev. Lett.* **50**, 2086 (1983).
- [10] S. Ichimaru, H. Iyetomi, and S. Tanaka, *Phys. Rep.* **149**, 91 (1987).
- [11] J. J. Bollinger and D. J. Wineland, *Phys. Rev. Lett.* **53**, 348 (1984).
- [12] S. L. Gilbert, J. J. Bollinger, and D. J. Wineland, *Phys. Rev. Lett.* **60**, 2022 (1988).
- [13] M. J. Stevens and M. O. Robbins, *J. Chem. Phys.* **98**, 2319 (1993).
- [14] R. T. Farouki and S. Hamaguchi, *J. Chem. Phys.* **101**, 9885 (1994).
- [15] S. Hamaguchi, R. T. Farouki, and D. H. E. Dubin, *J. Chem. Phys.* **105**, 7641 (1996).
- [16] S. Hamaguchi, R. T. Farouki, and D. H. E. Dubin, *Phys. Rev. E* **56**, 4671 (1997).
- [17] P. Hartmann, G. J. Kalman, Z. Donkó, and K. Kutasi, *Phys. Rev. E* **72**, 026409 (2005).
- [18] C. A. Murray, W. O. Sprenger, and R. A. Wenk, *Phys. Rev. B* **42**, 688 (1990).
- [19] C. A. Murray and D. G. Grier, *Annu. Rev. Phys. Chem.* **47**, 421 (1996).
- [20] J. H. Chu and Lin I, *Phys. Rev. Lett.* **72**, 4009 (1994).
- [21] Y. Hayashi and S. Tachibana, *Jpn. J. Appl. Phys.* **33**, L804 (1994).
- [22] H. Thomas, G. E. Morfill, V. Demmel, J. Goree, B. Feuerbacher, and D. Möhlmann, *Phys. Rev. Lett.* **73**, 652 (1994).
- [23] M. Wolter and A. Melzer, *Phys. Rev. E* **71**, 036414 (2005).
- [24] V. Nosenko, J. Goree, and A. Piel, *Phys. Plasmas* **13**, 032106 (2006).
- [25] C. A. Murray and D. H. Van Winkle, *Phys. Rev. Lett.* **58**, 1200 (1987).
- [26] C. A. Murray and R. A. Wenk, *Phys. Rev. Lett.* **62**, 1643 (1989).
- [27] K. Zahn, R. Lenke, and G. Maret, *Phys. Rev. Lett.* **82**, 2721 (1999).
- [28] M. A. Stan and A. J. Dahm, *Phys. Rev. B* **40**, 8995 (1989).
- [29] D. J. Bishop, W. O. Sprenger, R. Pindak, and M. E. Neubert, *Phys. Rev. Lett.* **49**, 1861 (1982).
- [30] J. S. Olafsen and J. S. Urbach, *Phys. Rev. Lett.* **95**, 098002 (2005).
- [31] R. Seshadri and R. M. Westervelt, *Phys. Rev. B* **46**, 5150 (1992).
- [32] F. Boyer and E. Falcon, *Phys. Rev. Lett.* **103**, 144501 (2009).
- [33] I. Guillamón, H. Suderow, A. Fernández-Pacheco, J. Sesé, R. Córdoba, J. M. De Teresa, M. R. Ibarra, and S. Vieira, *Nat. Phys.* **5**, 651 (2009).
- [34] K. J. Strandburg, *Rev. Mod. Phys.* **60**, 161 (1988).
- [35] A. V. Ivlev, U. Konopka, G. Morfill, and G. Joyce, *Phys. Rev. E* **68**, 026405 (2003).
- [36] D. Samsonov, S. K. Zhdanov, R. A. Quinn, S. I. Popel, and G. E. Morfill, *Phys. Rev. Lett.* **92**, 255004 (2004).
- [37] T. E. Sheridan, *Phys. Plasmas* **15**, 103702 (2008).
- [38] V. Nosenko, S. K. Zhdanov, A. V. Ivlev, C. A. Knapek, and G. E. Morfill, *Phys. Rev. Lett.* **103**, 015001 (2009).
- [39] Y. Feng, J. Goree, and B. Liu, *Phys. Rev. Lett.* **104**, 165003 (2010).

- [40] H. M. Thomas and G. E. Morfill, *Nature (London)* **379**, 806 (1996).
- [41] A. Melzer, A. Homann, and A. Piel, *Phys. Rev. E* **53**, 2757 (1996).
- [42] R. A. Quinn and J. Goree, *Phys. Rev. E* **64**, 051404 (2001).
- [43] Y. J. Lai and Lin I, *Phys. Rev. Lett.* **89**, 155002 (2002).
- [44] R. Ichiki, Y. Ivanov, M. Wolter, Y. Kawai, and A. Melzer, *Phys. Rev. E* **70**, 066404 (2004).
- [45] J. M. Kosterlitz and D. J. Thouless, *J. Phys. C* **6**, 1181 (1973).
- [46] B. I. Halperin and D. R. Nelson, *Phys. Rev. Lett.* **41**, 121 (1978).
- [47] D. R. Nelson and B. I. Halperin, *Phys. Rev. B* **19**, 2457 (1979).
- [48] A. P. Young, *Phys. Rev. B* **19**, 1855 (1979).
- [49] M. A. Glaser and N. A. Clark, *Phys. Rev. A* **41**, 4585 (1990).
- [50] M. A. Glaser and N. A. Clark, *Adv. Chem. Phys.* **83**, 543 (1993).
- [51] M. A. Glaser and N. A. Clark, in *Proceedings of the Fourth Nishinomiya-Yukawa Memorial Symposium, Dynamics and Patterns in Complex Fluids*, edited by A. Onuki and M. Doi (Springer, Berlin, 1993).
- [52] G. F. Voronoi, *J. Reine Angew. Math.* **136**, 67 (1909).
- [53] Y. Feng, J. Goree, and B. Liu, *Phys. Rev. Lett.* **100**, 205007 (2008).
- [54] See supplemental material at [<http://link.aps.org/supplemental/10.1103/PhysRevE.83.066402>] for source codes in two programming languages.
- [55] B.-J. Lin and L.-J. Chen, *J. Chem. Phys.* **126**, 034706 (2007).
- [56] Z. Wang, A. M. Alsayed, A. G. Yodh, and Y. Han, *J. Chem. Phys.* **132**, 154501 (2010).
- [57] V. Nosenko and S. K. Zhdanov, *Contrib. Plasma Phys.* **49**, 191 (2009).
- [58] C.-L. Chan, C.-W. Io, and Lin I, *Contrib. Plasma Phys.* **49**, 215 (2009).
- [59] O. Arp, D. Block, A. Piel, and A. Melzer, *Phys. Rev. Lett.* **93**, 165004 (2004).
- [60] J. D. Bernal, *Nature (London)* **183**, 141 (1959).
- [61] J. D. Bernal, *Nature (London)* **185**, 68 (1960).
- [62] C. Liu, S. Yamazaki, R. Hobara, I. Matsuda, and S. Hasegawa, *Phys. Rev. B* **71**, 041310(R) (2005).
- [63] U. Konopka, G. E. Morfill, and L. Ratke, *Phys. Rev. Lett.* **84**, 891 (2000).
- [64] Y. Feng, J. Goree, and B. Liu, *Rev. Sci. Instrum.* **78**, 053704 (2007).
- [65] P. Hartmann, A. Douglass, J. C. Reyes, L. S. Matthews, T. W. Hyde, A. Kovács, and Z. Donkó, *Phys. Rev. Lett.* **105**, 115004 (2010).